Contents lists available at ScienceDirect

Transactions of Nonferrous Metals Society of China

36(2026) 80−95

www.tnmsc.cn

Microstructure evolution and corrosion behavior of refill friction stir spot welding joint for dissimilar Al alloys

Fang-yuan JIANG [a,b], Da ZHANG [a,b], Yan-kun MA [a,b], Jiang-tao XIONG [a,b,*], Wei GUO [a,b,**], Jing-long LI [a,b]

[a] State Key Laboratory of Solidification Processing, Northwestern Polytechnical University, Xi'an 710072, China;
[b] Shaanxi Key Laboratory of Friction Welding Technologies, Northwestern Polytechnical University, Xi'an 710072, China

Abstract: The dissimilar 2B06 and 7B04 Al alloy joints were prepared by refill friction stir spot welding (RFSSW), and the microstructural evolution and corrosion behavior of the joints were investigated. Based on microstructural analysis, the welded joints exhibit distinct microstructural zones, including the stir zone (SZ), thermomechanically affected zone (TMAZ), and heat-affected zone (HAZ). The grain size of each zone is in the order of HAZ > TMAZ > SZ. Notably, the TMAZ and HAZ contain significantly larger secondary-phase particles compared to the SZ, with particle size in the HAZ increasing at higher rotational speeds. Electrochemical tests indicate that corrosion susceptibility follows the sequence of HAZ > TMAZ > SZ > BM, with greater sensitivity observed at increased rotational speeds. Post-corrosion mechanical performance degradation primarily arises from crevice corrosion at joint overlaps, but not from the changes in the microstructure.

Keywords: refill friction stir spot welding; high strength Al alloy; dissimilar joint; microstructure evolution; corrosion behavior

1 Introduction

High-strength 2xxx and 7xxx series Al alloys are widely used in aircraft structure manufacturing due to their high specific strength [1−3]. However, physical property differences between these alloys often lead to metallurgical defects [4], such as pores, inclusions, and thermal cracks, during fusion welding [5−12], compromising weld quality and the reliability of dissimilar Al alloy joints. Additionally, joining Al alloys via riveting and bolting is labor-intensive and costly, making it impractical for many production environments [13]. Refill friction stir spot welding (RFSSW), an innovative solid-state spot joining technique derived from friction stir welding (FSW), has gained traction for effectively joining similar and dissimilar Al alloys and Al−Mg alloys [14−23]. Unlike fusion welding, RFSSW avoids metallurgical issues [24−28] and offers pollutant-free, energy-efficient, and high-strength bonding, making it suitable for the high-performance requirements in the aerospace industry [29].

The corrosion behavior of Al alloy RFSSW joints is closely related to the microstructural characteristics of the welded joint region. ZHANG et al [30,31] conducted separate studies on RFSSW joints involving 2524 and 7050 Al alloys. The experimental results revealed a clear correlation between the microstructural features of the joints and their macroscopic corrosion behavior. The continuity of the precipitated phase was identified as a crucial factor. The highest degree of continuous

Corresponding author: *Jiang-tao XIONG, E-mail: xiongjiangtao@nwpu.edu.cn; **Wei GUO, E-mail: nwpuweiguo@nwpu.edu.cn
https://doi.org/10.1016/S1003-6326(25)66950-0
Received 6 May 2024; accepted 28 November 2024

distribution of intergranular precipitated phases is found in the heat-affected zone (HAZ), where there is a high susceptibility to intergranular corrosion and exfoliation corrosion. However, there is currently limited research on the corrosion behavior of RFSSW joints involving dissimilar Al alloys, with most studies focusing on FSW. In an investigation of AA2024/7075 FSW joints, ZHANG et al [32−34] categorized micro-regions based on material mixing in the stir zone (SZ) and conducted extensive tests to assess corrosion resistance across regions. These findings suggest that sufficient material mixing in FSW can effectively reduce corrosion sensitivity. XU et al [35] investigated the impact of process parameters in single and double-side friction stir welding of AA7085−T7452 on stress corrosion cracking (SCC) sensitivity. The results revealed that a reduction in Cu content in the grain boundary precipitated phase of the FSW joint increases SCC sensitivity, thereby elevating the overall stress corrosion sensitivity of the joint. Further studies on SCC behavior in the SZ of the AA7075−T651 Al alloy FSW joint, were conducted by PARASURAMAN et al [36] and by MORETO et al [37] on the evolution of local corrosion with 2524-T3 post-FSW utilized techniques such as scanning vibration electrode technology (SVET) and pH micro-potential measurement. Results indicated that FSW decomposed larger alloy particles into smaller, more evenly distributed particles across the welded area, enhancing both corrosion fatigue and overall corrosion resistance. Additionally, DENG et al [38] investigated the microstructure evolution of the 2195 Al alloy FSW joint and its corrosion behavior. They concluded that the precipitation and redissolution of Cu-rich precipitates resulted in variations in the corrosion potential of the Al matrix between regions, leading to robust coupling of macro-electric couple between regions and minimal pitting sensitivity in the HAZ.

In summary, the current common characteristics for the evolution of microstructure in high-strength Al alloy RFSSW joints remain insufficiently understood, including the variation in corrosion potential across joint regions and the macroscopic direction of galvanic coupling corrosion. Moreover, the correlation between the microstructure characteristics of the joints and the macroscopic corrosion behavior has not been established. It hinders the provision of sufficient theoretical and technical support for corrosion protection. Therefore, it is of great significance to analyze the relationship between microstructural characteristics and macroscopic corrosion behavior of dissimilar RFSSW joints.

2 Experimental

In this experiment, dynamic gantry-type refill stir friction spot welding equipment was utilized, as depicted in Figs. 1(a, b). The welding tool consists of three components: the stirring pin, stirring shoulder, and compression ring, as illustrated in Fig. 1(c). The stirring pin has a diameter of 6 mm, the shaft shoulder has a diameter of 9 mm, and the compression ring has a diameter of 13 mm.

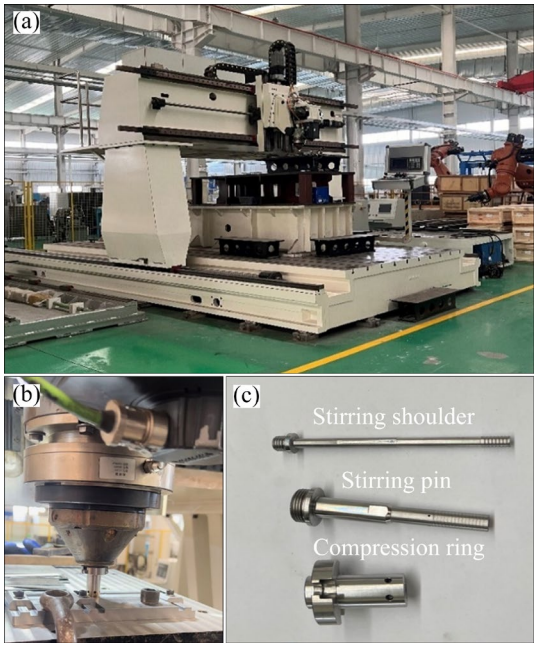

Fig. 1 Refill friction stir spot welding (RFSSW) equipment and tool: (a) RFSSW equipment; (b) RFSSW equipment welding area; (c) RFSSW stirring tool

In this experiment, 2B06 and 7B04 Al alloys were selected as base materials, with their chemical compositions given in Table 1. The 2B06 alloy, part of the Al−Cu−Mg series, is a heat-resistant structural material offering excellent properties, including plasticity and fracture toughness. The 7B04 alloy, a high-strength Al−Zn−Mg−Cu alloy, has substantial tensile strength, and an effective response to heat treatment. The 2B06 alloy was prepared in the T42 temper, while the 7B04 alloy was treated in the T74 temper. Figure 2 depicts the

lap joint test configuration for these alloys, with the specimen dimensions of 100 mm × 25 mm × 1 mm and 100 mm × 25 mm × 1.5 mm, respectively. Table 2 summarizes the RFSSW process parameters used in the welding trials.

Table 1 Nominal chemical compositions of 2B06 and 7B04 Al alloy (wt.%)

Alloy	Al	Cu	Mg	Mn	Fe	Si	Zn	Ti
2B06	Bal.	4.3	2.3	0.2	0.3	0.2	0.1	0.1
7B04	Bal.	2.0	2.8	0.6	0.2	0.1	6.5	0.1

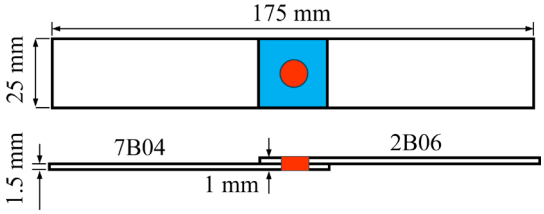

Fig. 2 Design of dissimilar Al alloy 2B06/7B04 joint

Table 2 Process parameters of refill friction stir spot welding

No.	Speed/ ($r \cdot min^{-1}$)	Plunge depth/mm	Plunge rate/ ($mm \cdot min^{-1}$)	Refill rate/ ($mm \cdot min^{-1}$)
1	1600	1.6	60	60
2	1900	1.6	60	60
3	2200	1.6	60	60

After welding, samples were polished using SiC sandpaper and a diamond polishing agent (particle size: 2.5 μm). Metallurgical specimens were etched with Keller's reagent (2.5 mL HNO_3 + 1.5 mL HCl + 1 mL HF + 95 mL H_2O) to prepare for morphological analysis. First, the macroscopic distribution of the grain structure was observed with an optical metallurgical microscope. Grain structure characteristics were then acquired using an electron backscatter diffraction (EBSD) probe integrated with a field emission scanning electron microscope (SEM). A back-scattered electron detector on the SEM was used to characterize the size and distribution of secondary-phase particles at the micrometer level. Following these analyses, tensile shear tests were performed on an electronic universal testing machine. Plates matching the base metal thickness were mounted on each side of the tensile shear sample at the chuck positions to ensure parallel force application. The tensile test was conducted at a constant rate of 1 mm/min, with displacement−load data recorded throughout.

Subsequently, the electrochemical behavior of each zone of the joint was characterized using the three-electrode electrochemical workstation. The measurement area was 3 mm × 4 mm. The Ag/AgCl electrode was used as a reference electrode. The Pt electrode was used as an auxiliary electrode, and each designated study area was used as a working electrode. The working electrode was immersed in a 3.5 wt.% NaCl electrolyte for 30 min to monitor the variation in the open circuit potential (OCP) of the electrode. Once the open circuit potential stabilized, the AC impedance (EIS) was measured within the frequency range of 0.1−10000 Hz. Subsequently, a polarization current of 10 mV (at the open circuit potential) was applied, and the polarization curve of the working electrode was measured within the range of ±100 mV (relative to the open circuit potential) at a scanning speed of 1 mV/s.

Finally, salt spray corrosion was used to simulate the marine atmospheric environment during the service of RFSSW joints. The corrosion medium was 5% NaCl solution and the corrosion temperature was room temperature. The changes of the macroscopic and microscopic corrosion morphology of the joint surface with time were observed after 72 h of corrosion.

3 Results and discussion

3.1 Evolution of grain structure

The surface morphology and cross-section morphology of the joints at various rotational speeds are shown in Fig. 3. The surface of each joint is well-formed, without a central exit hole or apparent forming defects. Moreover, an increase in rotational speed correlates with an expansion of SZ region. This phenomenon occurs due to the elevated welding speed leading to increased heat input, resulting in a more significant metal-plastic flow. Additionally, as the speed increases, the height of the solder joint gradually decreases, and stickiness appears in the upper part of the SZ, forming a weak connection at high speed. This phenomenon is attributed to the high speed of the mixing head, leading to an increase in heat production per unit of time. During the evacuation stage of the mixing head, adhesion between the material and the mixing head occurs, resulting in the formation of pits on the surface of the solder joint.

Following the macroscopic morphological analysis of the joint, EBSD was employed for detailed observations in distinct regions. Figure 4 shows the inverse pole Figure (IPF) maps for the SZ and HAZ. The high-angle grain boundaries, identified by an orientation difference greater than 15°, are represented by a black line in the IPF diagram. The low-angle grain boundaries are characterized by an orientation difference angle of 2°−15°, depicted by a white line in the IPF diagram. Both 2B06 and 7B04 are heat-treated, rolled Al alloys, with the grain morphology of the base metal

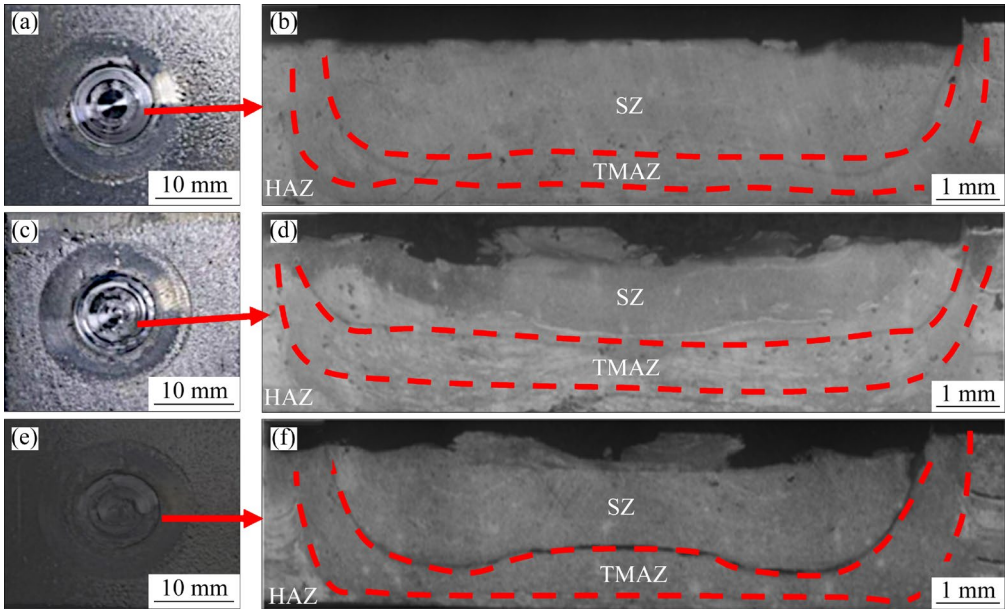

Fig. 3 Evolution of surface morphology and joint cross-section morphology with rotation speed: (a) 1600 r/min, surface morphology; (b) 1600 r/min, cross-section morphology; (c) 1900 r/min, surface morphology; (d) 1900 r/min, cross-section morphology; (e) 2200 r/min, surface morphology; (f) 2200 r/min, cross-section morphology

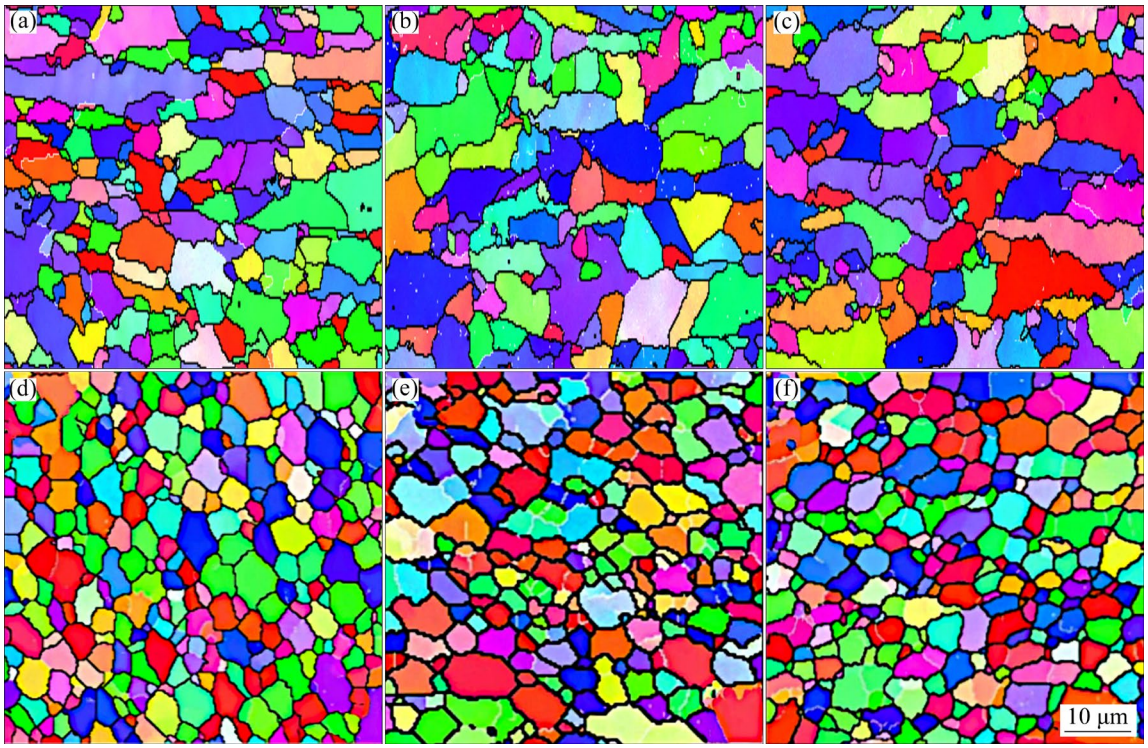

Fig. 4 EBSD images of 2B06/7B04 joints in different zones and at different speeds: (a) HAZ, 1600 r/min; (b) HAZ, 1900 r/min; (c) HAZ, 2200 r/min; (d) SZ, 1600 r/min; (e) SZ, 1900 r/min; (f) SZ, 2200 r/min

equiaxed along the rolling direction. The robust stirring action of the stirring tool induces friction heat generation in the SZ, leading to dynamic recrystallization and consequently resulting in a reduced grain size. Thermomechanically affected zone (TMAZ), situated at the periphery of the SZ, is primarily influenced by the insertion, refilling, and stirring of the shaft shoulder. These factors contribute to changes in the grain morphology within the TMAZ. The elongated grains exhibit an inclination towards the rolling direction of the base metal. However, the grain size near SZ is smaller, while the grain size near HAZ is equivalent to the HAZ due to reduced mechanical action. Due to heat input on the joint surface, the grains in the HAZ coarsen compared to those in the base metal (BM).

Figures 4(a−c) depict IPF diagrams of HAZ at varying speeds. Due to the weak mechanical action and predominant heat effect in the HAZ, the grain shape and size in this region are coarser than those of the base material, appearing as elongated strips. Table 3 presents the grain size statistics in the HAZ of the joint across various rotational speeds. At 1600 r/min, the anticipated grain size in the HAZ is the smallest at 17.47 μm. Conversely, at 2200 r/min, the expected grain size increases to 24.95 μm, with the maximum grain size reaching 108.11 μm. Figures 4(d−f) represent IPF at varying speeds in the SZ. The diagrams indicate a decrease in grain size in the SZ due to mechanical agitation, resulting in a uniform distribution. At 1600 r/min, 50% of the grain size of SZ falls within the 2−4 μm range. At 1900 r/min, significant growth in grain size occurs in the SZ. This growth is primarily attributed to the larger joint heat input, extended high-temperature residence time, and elevated temperature associated with high rotational speed, leading to grain growth through recrystallization. Additionally, the grain size range exhibits a wide distribution, with the primary grain size concentrated in the 2−10 μm range. At a welding speed of 2200 r/min, the SZ zone features a higher prevalence of small-sized grains, concentrated in the 0−4 μm range. Specifically, the grain size distribution shows that 27% fall within the 0−2 μm range, and 51% fall within the 2−4 μm range.

Table 3 Grain size in HAZ of Al alloy 2B06/7B04 joints at different speeds

Speed/ ($r \cdot min^{-1}$)	Grain size/μm		
	Average	Maximum	Minimum
1600	17.47	81.65	1.69
1900	19.88	83.81	1.35
2200	24.95	108.11	1.69

To gain deeper insights into the phase composition and distribution of the RFSSW joint, SEM and EDS analyses were conducted. As depicted in Fig. 5, SEM scanning images provide a detailed view of each area of the joint. Based on the analysis of the test results, SZ exhibits large white areas and small dots. Composition analysis reveals a high Zn content with x(Mg):x(Zn)≈1:2 in the SZ,

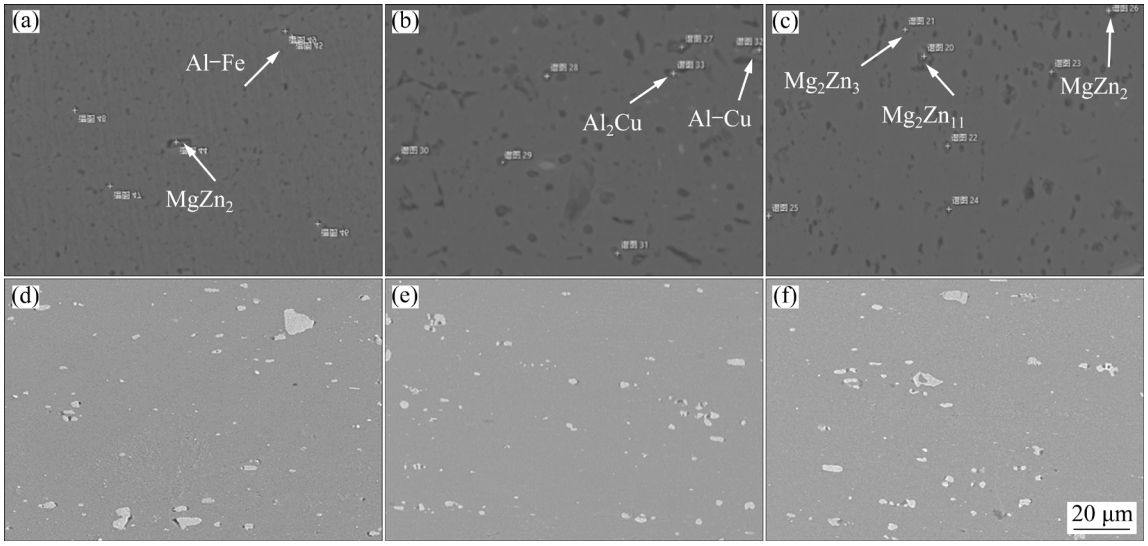

Fig. 5 Distribution of secondary-phase particles in 2B06/7B04 Al alloy joints in different regions and at different speeds: (a) SZ, 1600 r/min; (b) TAMZ, 1600 r/min; (c) HAZ, 1600 r/min; (d) HAZ, 1600 r/min; (e) HAZ, 1900 r/min; (f) HAZ, 2200 r/min

initially identified as an accumulation area of $MgZn_2$. Additionally, a region with x(Al):x(Fe)≈1:1, sized less than 1 μm, may form during the welding process of intermetallic compounds. Within the HAZ corrosion pit, massive particles with x(Al):x(Cu)=2:1, identified as the strengthening phase θ(Al_2Cu), are discovered. Additionally, x(Al):x(Cu)=7:1 is observed, representing the Al−Cu matrix. The TMAZ region also reveals Fe-based particles, as well as phases such as Al_2Cu, Mg_2Zn, Mg_2Zn_{11}, and Mg_2Zn_3. Figures 5(d−f) illustrate the distribution of precipitated phases in the HAZ at various welding speeds. Size statistics of secondary-phase particles in the HAZ indicate that, with the increase of rotational speed, these particles are coarsened, accompanied by a decrease in their overall number.

3.2 Local electrochemical behavior of joint

In the corrosive environment, the welding area frequently exhibits varying open circuit potential, leading to macroscopic galvanic corrosion across specific regions. Figure 6(a) depicts the temporal evolution of the open circuit potential within each welding area of the 2B06/7B04 Al alloy joint. The corrosive medium used was a 3.5% NaCl solution. The designated testing area was immersed in the corrosive medium for 1 h before the test to ensure a stabilized electrode reaction. Examination of Fig. 6(a) reveals that the open circuit potential of the SZ is centrally located, with a limited fluctuation range. The open circuit potential in the TMAZ and HAZ regions is lower than that in SZ, whereas the BM region exhibits the highest potential with the widest fluctuation range. This observation indicates that the HAZ and TMAZ exhibit the highest level of electrochemical sensitivity. Consequently, within the corrosive environment of the 2B06/7B04 Al alloy joint, the BM acts as the cathode, while the HAZ or TMAZ functions as the anode, initiating macro-galvanic corrosion and leading to accelerated dissolution in these regions. Figure 6(b) illustrates the polarization curves of 2B06/7B04 Al alloy joints for the SZ, TMAZ, HAZ, and BM in corrosive media. A passivation platform is not observed in all the curves, which indicates that pitting corrosion develops in conjunction with current fluctuations. The ordering of corrosion potentials in each region is BM > SZ > TMAZ > HAZ, which is consistent

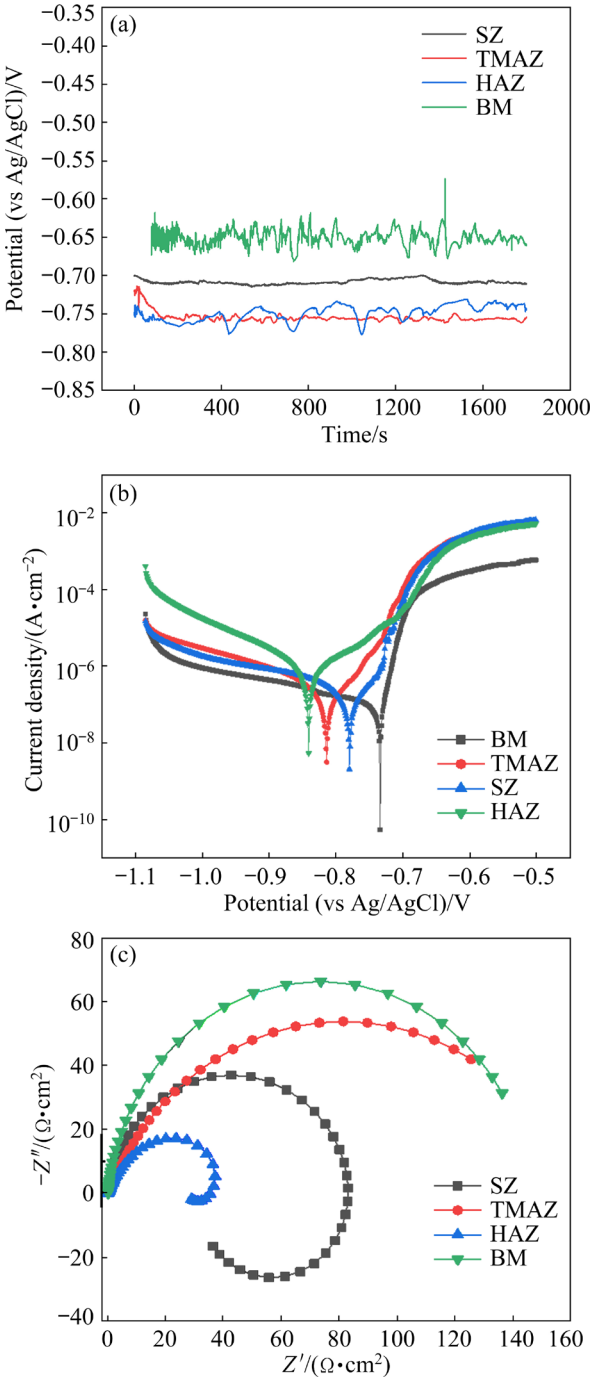

Fig. 6 Test results of electrochemical behavior in connection area of 2B06/7B04 Al alloy: (a) Open circuit potential of each region; (b) Polarization curves of each region; (c) Impedance diagrams of each region

with the results of the open circuit potential test. The examination of Fig. 6(b) reveals that the polarization curve for each welding region of the joint follows a consistent trend. The absolute value of the slope in the anode region significantly exceeds 0, whereas the slope in the cathode region remains close to 0 across a considerable range. The

findings indicate that in a neutral corrosion solution containing Cl^-, the primary corrosion mechanism for the 2B06/7B04 Al alloy joint is oxygen absorption corrosion. The severity of corrosion increases with the oxygen content in the corrosion solution. Table 4 presents the electrochemical parameters for each region of the joint. The self-corrosion potential of BM is the highest at −0.53 V, accompanied by the lowest self-corrosion current density at 1.0×10^{-7} A/cm^2. The ranking of corrosion current density in various areas of the joint is as follows: HAZ > SZ > TMAZ > BM, with the current density in the HAZ being significantly higher than that in other regions. Corrosion current density is proportional to the corrosion rate: the higher the current density, the faster the corrosion rate, and the worse the corrosion resistance of the material. Based on a comprehensive analysis of the polarization curve results, the corrosion resistance of the joint regions is ranked as follows: BM > SZ > TMAZ > HAZ. Figure 6(c) illustrates the AC impedance diagram for the various areas of joint. Examination of Fig. 6(c) reveals that the AC impedance of the BM and TMAZ comprises a capacitor arc. The SZ resembles the HAZ, with the addition of a reactance-induced arc at low frequencies, indicative of active pitting in the system. A larger arc radius in the impedance diagram corresponds to increased polarization resistance, decreased corrosion current density, and enhanced corrosion resistance of the material. Consequently, based on the arc radius of the capacitive reactance, the order of corrosion resistance for different regions is established as follows: BM > TMAZ > SZ > HAZ.

Table 4 Electrochemical parameter of each zone in joint prepared by RFSSW on 2B06/7B04 Al alloy

Region	Self-corrosion potential, φ_{corr} (vs Ag/AgCl)/V	Self-corrosion current density, J_{corr}/(A·cm^{-2})
SZ	−0.74	3.21×10^{-7}
TMAZ	−0.81	2.52×10^{-7}
HAZ	−0.87	8.90×10^{-7}
BM	−0.53	1.00×10^{-7}

The total impedance of a basic electrochemical process can be represented by a circuit consisting of three electrical components: internal resistance (R_s), charge transfer resistance (R_t), double-layer capacitance (CPE), and Faraday impedance (R_p), as illustrated in Fig. 7. Internal resistance (R_s) primarily comprises the internal resistance of the electrolyte and the electrode. The double electric layer capacitor (CPE) originates from inactive ions in the electrolyte, causing no chemical reaction but altering the charge distribution. Faraday impedance (R_p) results from the REDOX reaction in the electrolyte, involving charge transfer processes. To further explain the corrosion mechanism, the equivalent corrosion circuits for different regions are depicted in Figs. 7(b, c). In Fig. 7(b), the equivalent circuit diagram represents BM and TMAZ, while Fig. 7(c) illustrates the equivalent circuit diagram for SZ and HAZ. In Fig. 6(c), Z' and Z'' respectively correspond to the real and imaginary parts of the impedance. Z' and Z'' can be expressed using Eqs. (1) and (2):

$$Z' = R_s + \frac{R_p + \sigma\omega^{-1/2}}{(C\sigma\omega^{1/2}+1)^2 + \omega^2 C^2 (R_p + \sigma\omega^{-1/2})^2} \quad (1)$$

$$Z'' = \frac{\omega C\left(R_p + \sigma\omega^{-1/2}\right) + \sigma\omega^{-1/2}(C\sigma\omega^{1/2}+1)}{(C\sigma\omega^{1/2}+1)^2 + \omega^2 C^2 (R_p + \sigma\omega^{-1/2})^2} \quad (2)$$

where C represents the value of the double-layer capacitance (CPE), ω is the angular frequency of

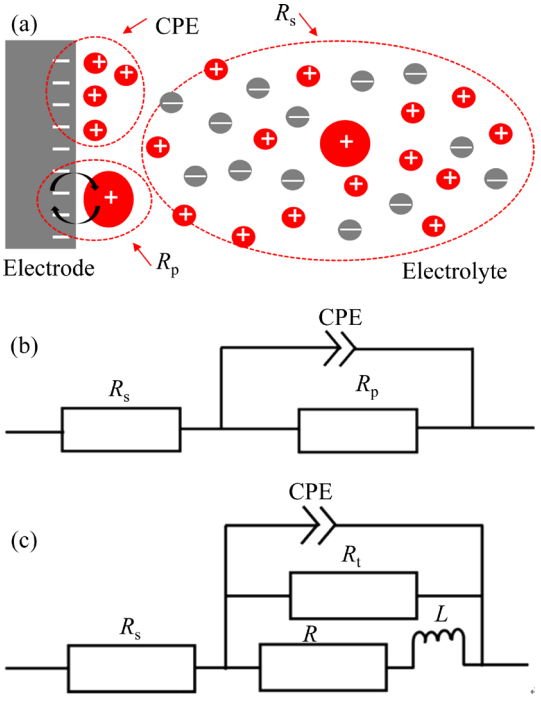

Fig. 7 Schematic diagram of electrochemical test process: (a) Schematic diagram of electrochemical process impedance; (b) Equivalent circuit models for BM and TMAZ; (c) Equivalent circuit models for SZ and HAZ

the sine wave signal, and σ is a coefficient associated with the material transfer. The pertinent electrochemical parameters acquired through fitting and calculating the AC impedance diagram for each welding area is presented in Table 5. By comparing the polarization resistance across different regions, it is evident that the order of polarization resistance for these regions is: BM > TMAZ > SZ > HAZ. Greater polarization resistance corresponds to lower corrosion current density and improved corrosion resistance of the material. Therefore, the corrosion resistance of the 2B06/7B04 Al alloy joints in different regions can be ranked according to the magnitude of the polarization resistance. This result is the same as the result of corrosion resistance determined by polarization curves.

3.3 Overall corrosion behavior

The joint underwent a neutral salt spray corrosion test to simulate a marine atmosphere aiming to validate the electrochemical sensitivity assessment and examine corrosion characteristics of the welded structure under simulated service conditions. Figure 8 displays the corrosion morphology of the 2B06/7B04 Al alloy joint section after up to 72 h of salt spray exposure. The sample's corrosion evolves progressively, with the joint surface losing its metallic luster and turning gray-black. A transparent gel forms on the surface, which dries to a white powder, with some areas showing white corrosion spots. In Fig. 8(b), a locally enlarged image of the SZ reveals a layer of thin and dense corrosion products covering this area. These products are fine, thin, and resemble fine sand. In Fig. 8(c), a locally enlarged image of the TMAZ region indicates that the corrosion products on its surface are noticeably thicker than those in the SZ. These corrosion products are loose and accumulate in bulk. In some areas, the corrosion products exhibit cracks and appear as irregular clumps. In Fig. 8(d), a locally enlarged image of the HAZ region reveals that the corrosion products on its surface become loose. The region is covered with a thin and loose white layer of corrosion products, some of which are cracked into irregular sheets with deep cracks.

Further characterization of the joint's corrosion morphology is presented. Figure 9 illustrates the surface corrosion morphology of the SZ. Upon observation, corrosion appears uniform across most areas of the SZ surface, with only a few pits, and their number is limited. The joint's surface is flat, as depicted in Fig. 9(b). Three prominent corrosion pits were selected, and their depths were measured, with results presented in Fig. 9(d). Among these, the 3# corrosion pit reaches a maximum depth of 3.85 μm. As shown in Fig. 10, the surface corrosion morphology of the TMAZ in the joint reveals a higher corrosion degree compared to the SZ. This heightened corrosion is attributed to the presence of a larger precipitated phase in the TMAZ, where the Cu content of this phase surpasses that of the surrounding Al matrix. Consequently, the precipitated phase exhibits a higher corrosion potential, engaging in a galvanic reaction with the Al matrix. The Al substrate, with a lower potential, acts as the anode and is more susceptible to corrosion, leading to the formation of larger corrosion pits. The corrosion pit depth in the TMAZ is significantly greater than that in the SZ, with the 2# corrosion pit reaching the maximum depth of 13.37 μm. Figure 11 depicts the corrosion morphology of the HAZ. The number of corrosion pits in the HAZ is notably higher than that in the TMAZ and SZ. Statistical analysis of corrosion pit depths reveals that the 2# corrosion pit has the greatest depth, measuring 17.84 μm.

Based on the preceding discussion, the corrosion resistance of the 2B06/7B04 Al alloy joint in different areas is determined to be in the

Table 5 Electrochemical impedance parameters of different regions of welded joints

Region	CPE/($W^{-1}\cdot cm^{-2}\cdot s^{-n}$)	R_t/($\Omega\cdot cm^2$)	R/($\Omega\cdot cm^2$)	L/($H\cdot cm^2$)	R_p/($\Omega\cdot cm^2$)
SZ	2.32×10^{-4}	85.42	46.96	71.48	30.30
HAZ	54.5×10^{-4}	56.51	56.02	33.04	28.13
TMAZ	36.9×10^{-4}	–	–	–	146.61
BM	4.15×10^{-4}	–	–	–	162.20

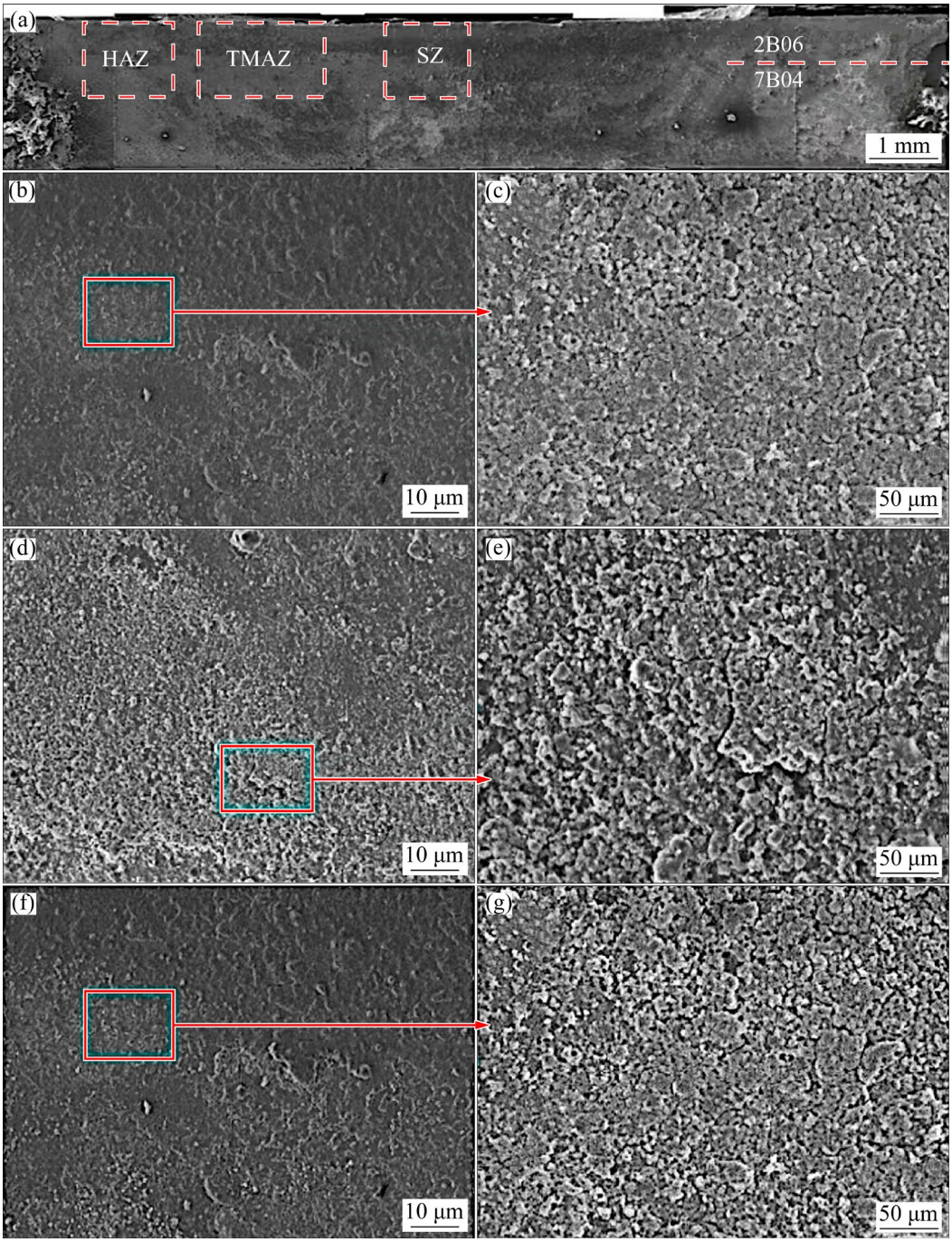

Fig. 8 SEM images of each zone of joints after salt spray corrosion: (a) Macrostructure of joint; (b, c) Microstructure of SZ; (d, e) Microstructure of TMAZ; (f, g) Microstructure of HAZ

following order: SZ > TMAZ > HAZ. The HAZ area exhibits severe corrosion, representing the weakest corrosion resistance among the joint's regions.

3.4 Effect of corrosion on mechanical property

The fracture morphologies of joints with different welding parameters are shown in Figs. 12−14. Upon comparison, it is evident that at a rotational speed of 1600 r/min, the fracture mode changes from the base metal fracture to the plug fracture before and after corrosion. All fractures exhibit a plug-type morphology. The mechanical properties of the joint were analyzed statistically, with results presented in Table 6. Notably, at a rotational speed of 1600 r/min, the tensile shear properties after corrosion are reduced to 97.67% of the original value, and the change in fracture mode

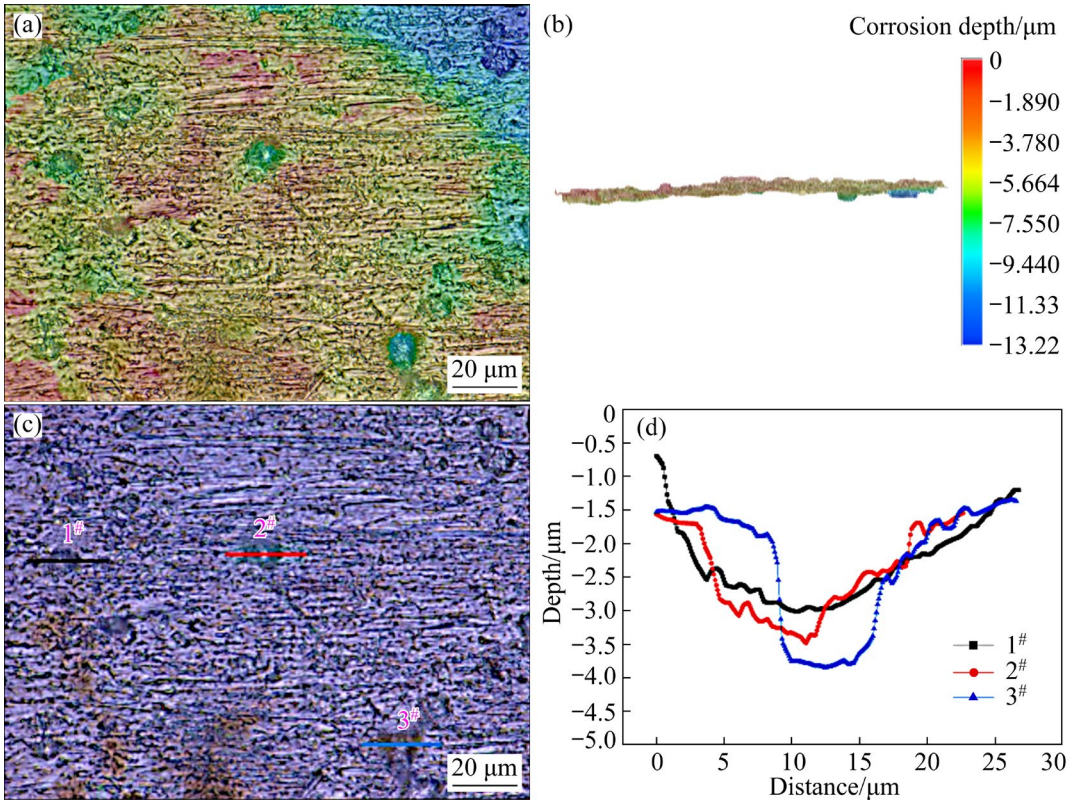

Fig. 9 Corrosion depth and corrosion morphology in SZ of joint after 72 h of salt spray corrosion: (a, b) Salt spray corrosion depth; (c) Corrosion morphology; (d) Salt spray corrosion depth curves

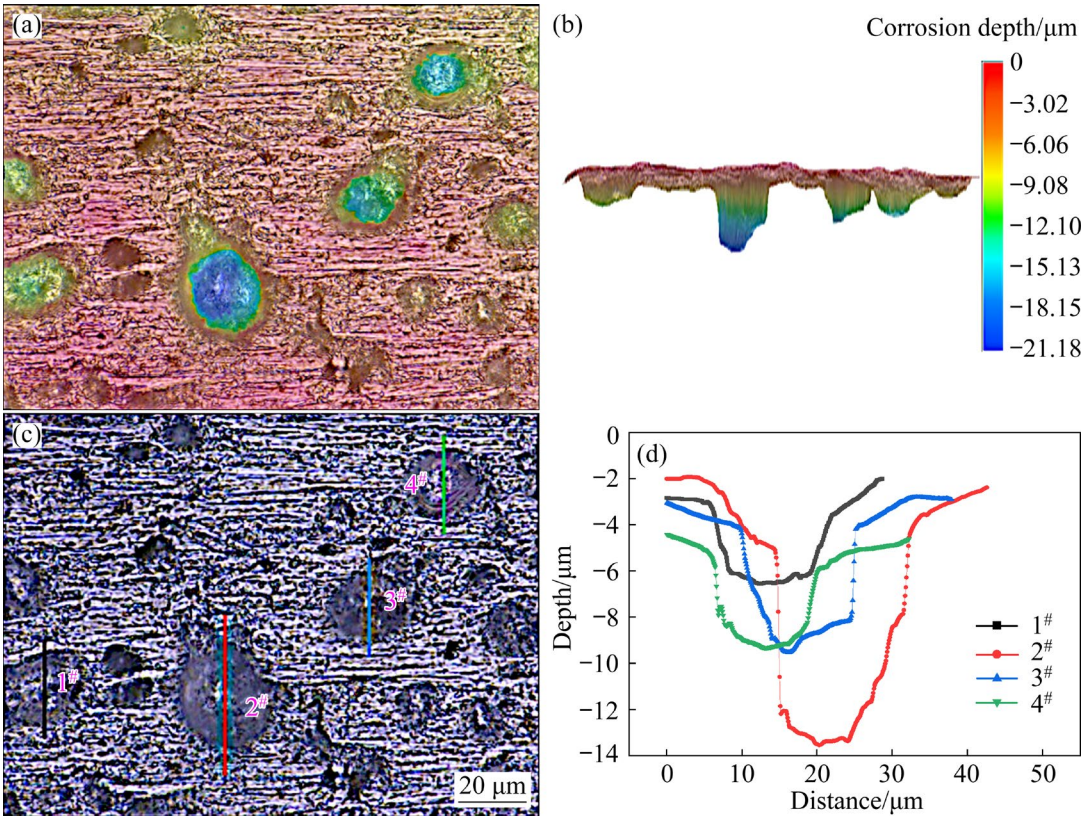

Fig. 10 Corrosion depth and corrosion morphology in TMAZ of joint after 72 h of salt spray corrosion: (a, b) Salt spray corrosion depth; (c) Corrosion morphology; (d) Salt spray corrosion depth curves

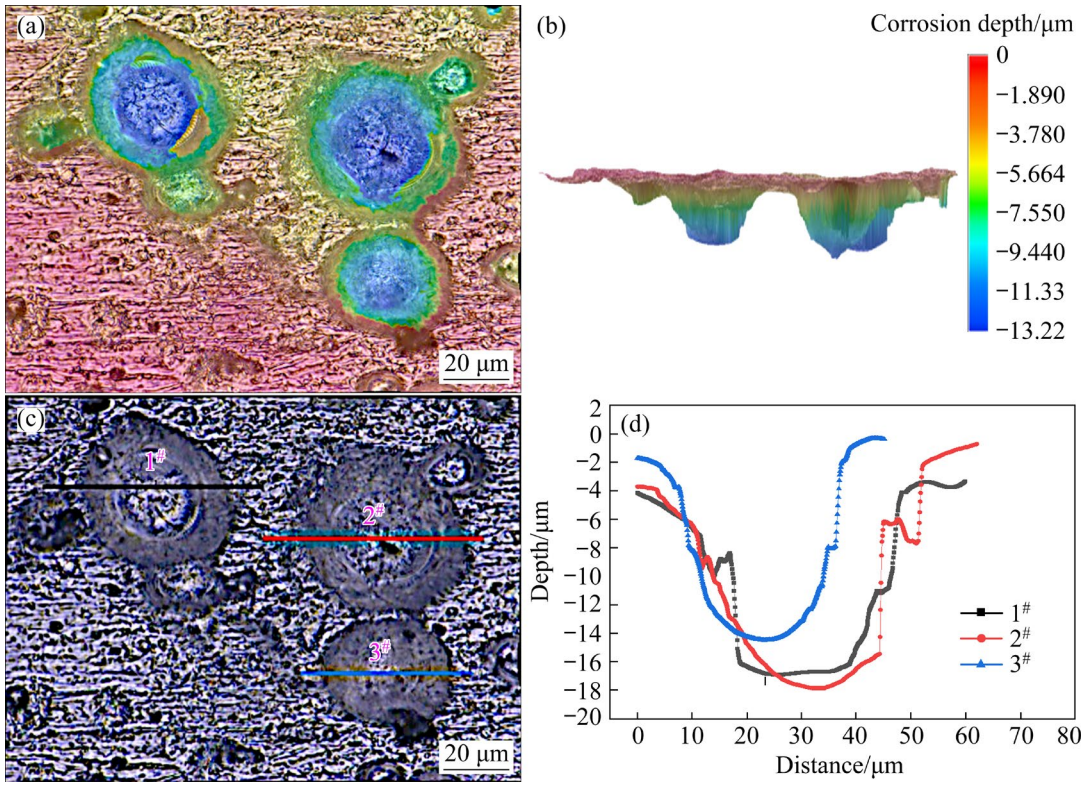

Fig. 11 Corrosion depth and corrosion morphology in HAZ of joint after 72 h of salt spray corrosion: (a, b) Salt spray corrosion depth; (c) Corrosion morphology; (d) Salt spray corrosion depth curves

has no significant impact on the joint's mechanical properties. However, at rotational speeds of 1900 and 2200 r/min, the mechanical properties of the joint are diminished, with the mechanical properties after corrosion reduced to 84.84% and 92.79%, respectively.

As illustrated in Figs. 12(d−g), the local magnification of A−D in the cross-section topography reveals lamellar tear topography at Position A, expanding downward along Position B. The joint's surface exhibits evident tearing edges and a flat fracture without obvious dimples, indicating a brittle fracture as the primary mode for the corroded joint. Before corrosion, the joint fractures at the 2B06 Al alloy base metal of the upper plate. After corrosion, the fracture position shifts to the HAZ region of the lower plate, and the fracture mode changes from the base metal fracture mode to the plug fracture mode.

The local amplification of A−C in the corroded cross-section topography at 1900 r/min is presented in Fig. 13. Position C corresponds to an area with a weld joint defect, and the interface exhibits a smooth and flat profile, indicating a weakly bonded region. During the tensile shear test, as the load gradually increases, the stress at the defect tip surpasses the critical stress, initiating crack propagation. Notably, a shallow and dense dimple is observed at Position B, signifying crack expansion under shear force. The interface cracks, forming a dimple and exhibiting a certain level of plasticity. At Position A, the fracture morphology is undulating and striated, resembling the river-like pattern characteristic of dissociation fracture, indicative of brittle fracture. In general terms, it can be classified as a mixed-type fracture.

The local amplification of A−C in the corroded cross-section topography at the rotational speed of 2200 r/min is depicted in Fig. 14. The crack initiates at Position C, displaying a smooth and flat profile, characteristic of brittle fracture. A substantial dimple is observed at Position A, and the crack extends to the joint's surface, forming a large shallow dimple on the surface, indicating a degree of plasticity. The corrosion of the crack has no impact on the fracture mode of the joint welded at 2200 r/min, maintaining a plug-type fracture both before and after corrosion.

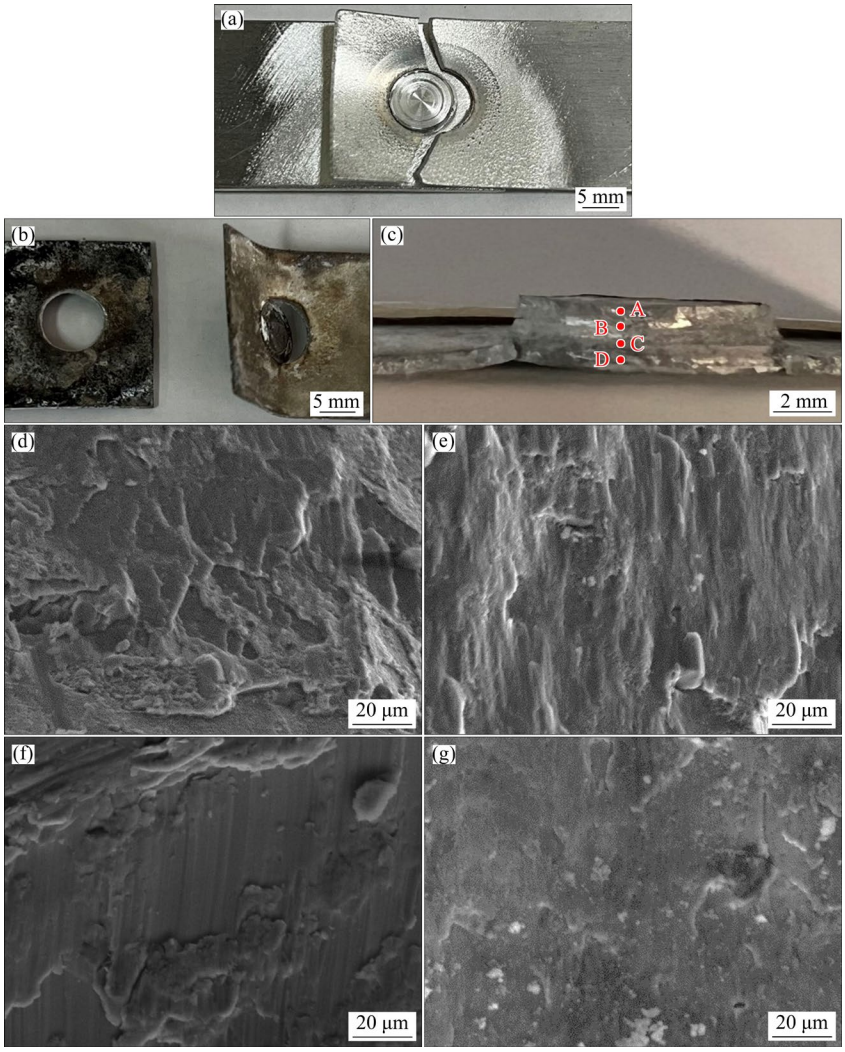

Fig. 12 Tensile-shear tested samples welded at 1600 r/min: (a) Photo of as-welded joint; (b) Photo of corroded joint; (c) Fractured surface of corroded joint; (d−g) Magnified images of Positions A, B, C, and D labeled on (c), respectively

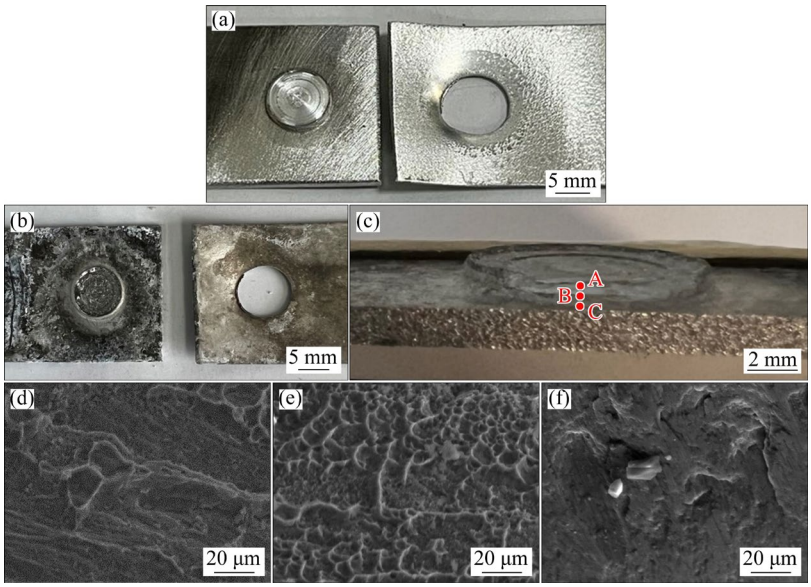

Fig. 13 Tensile-shear tested samples welded at 1900 r/min: (a) Photo of as-welded joint; (b) Photo of corroded joint; (c) Fractured surface of corroded joint; (d−f) Magnified images of Positions A, B and C labeled on (c), respectively

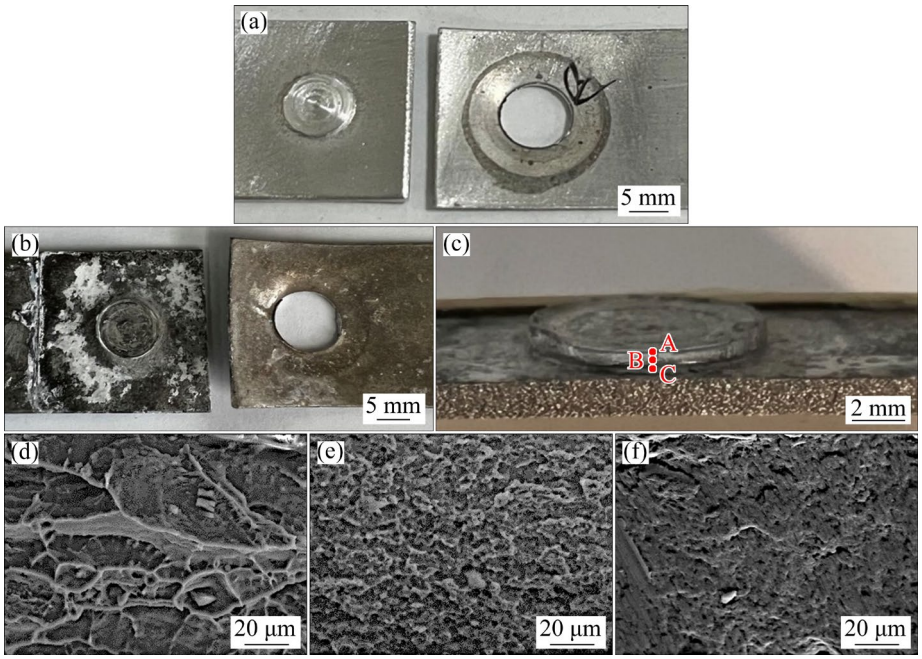

Fig. 14 Tensile-shear tested samples welded at 2200 r/min: (a) Photo of as-welded joint; (b) Photo of corroded joint; (c) Fractured surface of corroded joint; (d−f) Magnified images of Positions A, B and C labeled on (c), respectively

Table 6 Mechanical properties and fracture modes of joint prepared by RFSSW on 2B06/7B04 Al alloy before and after salt spray corrosion testing

Speed/ ($r \cdot min^{-1}$)	Pre-corrosion tensile shear load/kN	Pre-corrosion fracture mode	Post-corrosion tensile shear load/kN	Post-corrosion fracture mode
1600	5.15	Base metal type	5.03	Plug type
1900	4.09	Plug type	3.47	Plug type
2200	5.27	Plug type	4.89	Plug type

4 Discussion

Corrosion of welded joints is mainly caused by the electrochemical inhomogeneity of various regions of the weld. In a corrosive environment, a corrosion cell is formed between a high-potential region and a low-potential region. The potential difference among different regions creates a macroscopic galvanic coupling effect, where the low potential region is dissolved as an anode and the corrosion susceptibility becomes higher.

The primary precipitation phases in 2B06/7B04 Al alloy joints include the *S* phase (Al_2CuMg), θ phase (Al_2Cu), η phase ($MgZn_2$), and an irregular Al−Cu−Fe−Mn precipitation phase. These precipitated phases contain substantial amounts of Cu and Fe elements, and the corrosion potential of these precipitated phases is higher than that of the Al matrix. When the joint is in a neutral or acidic environment containing Cl^-, the Al matrix around the precipitated phase and the precipitated phase form a corrosion microcell, and the Al matrix is preferentially dissolved as the anode.

The SZ of the joint contains many secondary-phase particles, which exhibit a uniformly diffusive distribution. This distribution is attributed to the strong thermal-mechanical effects during welding, which induces dynamic recrystallization and results in the formation of small isometric crystals, replacing the flat grain morphology typical of rolled material. During this process, the secondary phase particles are fragmented. The average diameter of the secondary phase particles of SZ is exceedingly small and diffusively distributed with uniform chemical composition, so its corrosion sensitivity is low. In the TMAZ and HAZ, the thermal-mechanical effects of welding cause grain elongation, distortion, and growth, leading to the formation of inclined flat grains. The secondary-

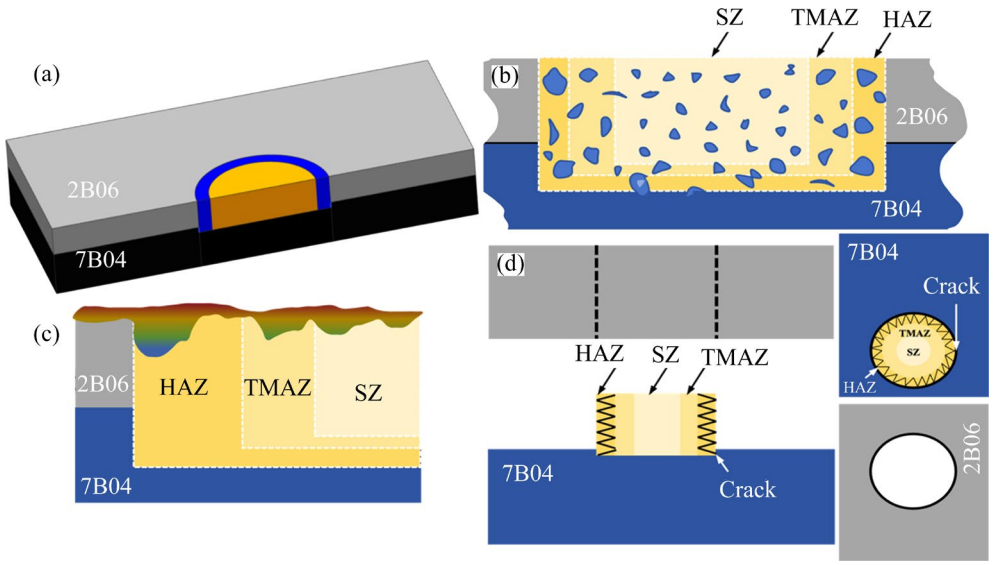

Fig. 15 Schematic diagram of microstructure and corrosion fracture of joints: (a) Al alloy RSSFW joint; (b) Secondary-phase distribution in joint; (c) Depth of corrosion in different regions of joint; (d) Fracture diagram of joint

phase particles are significantly coarsened, increased in size, and non-uniform. The microstructure and chemical composition here are grossly inhomogeneous, resulting in strong corrosion sensitivity in this region.

Pitting corrosion of Al alloy joints is a localized corrosion behavior concentrated in the anodic region, and the occurrence of corrosion is based on the continuous expansion of pitting on the metal surface. In a corrosive environment, the HAZ and TMAZ, due to their high corrosion sensitivity, function as anodes and corrode rapidly. The SZ and BM with low corrosion sensitivity become cathodes, and the corrosion is slow. The whole joint forms a macroscopic galvanic corrosion. After corrosion, the HAZ and TMAZ are significantly damaged. During tensile testing of the corroded joint, the fragile HAZ and TMAZ regions are the first to fail, leading to plug fracture. This is shown in Fig. 15.

5 Conclusions

(1) Based on microstructure differences, the joint is divided into three zones: the stir zone (SZ), the thermomechanically affected zone (TMAZ), and the heat-affected zone (HAZ). Grain size distribution follows the sequence: HAZ > TMAZ > SZ. Fine equiaxed grains are formed in the SZ due to dynamic recrystallization, while in the TMAZ, grains are elongated along the exit line, with some grains retaining a flattened shape aligned with the rolling direction. The grain morphology in the HAZ resembles that of the base metal (BM), with a slightly larger grain size.

(2) The size of the precipitated phase in different regions follows the order of HAZ ≈ TMAZ > BM > SZ. In the SZ, precipitated phase particles are fine and evenly distributed, while in the HAZ and TMAZ, they are coarser and unevenly distributed.

(3) The corrosion resistance of the joint is lower than that of the BM, making it more susceptible to corrosion as an anode. The HAZ exhibits the poorest corrosion resistance due to uneven local element distribution caused by the polarization of precipitated phases. The corrosion sensitivity of each region follows the order of HAZ > TMAZ > SZ > BM. With the rotational speed increasing, the polarization of precipitated phases is intensified, leading to progressively stronger corrosion. However, higher rotational speed reduces the overall corrosion sensitivity of the joint.

(4) In simulated marine atmospheric corrosion tests, severe crevice corrosion develops at the side laps of the joint. The corrosion significantly reduces the mechanical properties of the joint to a minimum of 84.84% of its pre-corrosion value. The microstructure of joints contributes to the corrosion and mechanical property degradation.

CRediT authorship contribution statement

Fang-yuan JIANG: Data curation, Investigation,

Formal analysis, Writing − Original draft; **Da ZHANG:** Writing − Review & editing; **Yan-kun MA:** Data curation; **Jiang-tao XIONG** and **Wei GUO:** Funding acquisition, Methodology; **Jing-long LI:** Supervision, Conceptualization.

Declaration of competing interest

The authors declare that they have no known competing financial interests or personal relationships that could have appeared to influence the work reported in this paper.

Acknowledgments

This work was supported by the National Natural Science Foundation of China (Nos. 52075449, 51975480).

References

[1] ÇAM G, MISTIKOGLU S. Recent developments in friction stir welding of Al-alloys [J]. Journal of Materials Engineering and Performance, 2014, 23: 1936−1953.

[2] LI Xiao-qiang, SONG Nan, GUO Gui-qiang. Experimental measurement and theoretical prediction of forming limit curve for Al alloy 2B06 [J]. Transactions of Nonferrous Metals Society of China, 2012, 22: s335−s342.

[3] LI Zhi-hui, XIONG Bai-qing, ZHANG Yong-an, ZHU Bao-hong, WANG Feng, LIU Hong-wei. Microstructural evolution of Al alloy 7B04 thick plate by various thermal treatments [J]. Transactions of Nonferrous Metals Society of China, 2008, 18: 40−45.

[4] MISHRA R S, MA Z Y. Friction stir welding and processing [J]. Materials Science and Engineering R: Reports, 2005, 50: 1−78.

[5] SUHUDDIN U, FISCHER V, KROEFF F, DOS SANTOS J F. Microstructure and mechanical properties of friction spot welds of dissimilar AA5754 Al and AZ31 Mg alloys [J]. Materials Science and Engineering A, 2014, 590: 384−389.

[6] SHEN Z, CHEN Y, HOU J S C, YANG X, GERLICH A P. Influence of processing parameters on microstructure and mechanical performance of refill friction stir spot welded 7075-T6 aluminum alloy [J]. Science and Technology of Welding and Joining, 2015, 20: 48−57.

[7] REILLY A, SHERCLIFF H, CHEN Y, PRANGNELL P. Modelling and visualization of material flow in friction stir spot welding [J]. Journal of Materials Processing Technology, 2015, 225: 473−484.

[8] CAO J Y, WANG M, KONG L, GUO L J. Hook formation and mechanical properties of friction spot welding in alloy 6061-T6 [J]. Journal of Materials Processing Technology, 2016, 230: 254−262.

[9] ZHAO Y, LIU H, YANG T, LIN Z, HU Y. Study of temperature and material flow during friction spot welding of 7B04-T74 Al alloy [J]. The International Journal of Advanced Manufacturing Technology, 2016, 83: 1467−1475.

[10] İPEKOĞLU G, ÇAM G. Formation of weld defects in cold metal transfer arc welded 7075-T6 plates and its effect on joint performance [J]. IOP Conference Series: Materials Science and Engineering, 2019, 629: 012007.

[11] ÇAM G. Prospects of producing Al parts by wire arc additive manufacturing (WAAM) [J]. Materials Today: Proceedings, 2022, 62: 77−85.

[12] ÇAM G, GÜNEN A. Challenges and opportunities in the production of magnesium parts by directed energy deposition processes [J]. Journal of Magnesium and Alloys, 2024, 12: 1663−1686.

[13] HINRICHS J F. Friction stir welding for the 21th Century automotive industry [C]//Proceedings of 5th International FSW symposium. Metz, France, 2004.

[14] TIER M D, ROSENDO T S, DOS SANTOS J F, HUBER N, MAZZAFERRO J A, MAZZAFERRO C P, STROHAECKER T R. The influence of refill FSSW parameters on the microstructure and shear strength of 5042 aluminum welds [J]. Journal of Materials Processing Technology, 2013, 213(6): 997−1005.

[15] AMANCIO-FILHO S T, CAMILLO A P, BERGMANN L, DOS SANTOS J F, KURY S E, MACHADO N G. Preliminary investigation of the microstructure and mechanical behaviors of 2024 aluminum alloy friction spot welds [J]. Materials Transactions, 2011, 52(5): 985−991.

[16] SCHILLING C, DOS SANTOS J. Method and device for joining at least two adjoining work pieces by friction welding: U.S. Patent 6,722,556 [P]. 2004−4−20.

[17] KHALIQ U A, MUHAMAD M R, YUSOF F, IBRAHIM S, ISA M S M, CHEN Z, ÇAM G. A review on friction stir butt welding of aluminum with magnesium: A new insight on joining mechanisms by interfacial enhancement [J]. Journal of Materials Research and Technology, 2023, 27: 4595−4624.

[18] AHMED M M, SELEMAN M M E S, FYDRYCH D, GÜREL Ç A M. Review on friction stir welding of dissimilar magnesium and aluminum alloys: Scientometric analysis and strategies for achieving high-quality joints [J]. Journal of Magnesium and Alloys, 2023, 11: 4082−4127.

[19] AHMED M M, EL-SAYED SELEMAN M M, FYDRYCH D, ÇAM G. Friction stir welding of Al in the aerospace industry: The current progress and state-of-the-art review [J]. Materials, 2023, 16(8): 2971.

[20] ÇAM G, JAVAHERI V, HEIDARZADEH A. Advances in FSW and FSSW of dissimilar Al-alloy plates [J]. Journal of Adhesion Science and Technology, 2023, 37(2): 162−194.

[21] KASHAEV N, VENTZKE V, ÇAM G. Prospects of laser beam welding and friction stir welding processes for Al airframe structural applications [J]. Journal of Manufacturing Processes, 2018, 36: 571−600.

[22] ÇAM G, İPEKOĞLU G. Recent developments in joining of Al alloys [J]. The International Journal of Advanced Manufacturing Technology, 2017, 91: 1851−1866.

[23] ÇAM G. Friction stir welded structural materials: Beyond Al-alloys [J]. International Materials Reviews, 2011, 56(1): 1−48.

[24] ZHANG C, CUI L, WANG D, LIU Y, LIU C, LI H. The heterogeneous microstructure of heat affect zone and its effect on creep resistance for friction stir joints on 9Cr−1.5W heat resistant steel [J]. Scripta Materialia, 2019, 158: 6−10.

[25] MA Z Y, FENG A H, CHEN D L, SHEN J. Recent advances in friction stir welding/processing of Al alloys: Microstructural evolution and mechanical properties [J]. Critical Reviews in Solid State and Materials Sciences, 2018, 43(4): 269−333.
[26] YANG C, WANG B B, YU B H, WU L H, XUE P, ZHANG X M, HE G Z, NI D R, XIAO B L, WANG K S, MA Z Y. High-cycle fatigue and fracture behavior of double-side friction stir welded 6082Al ultra-thick plates [J]. Engineering Fracture Mechanics, 2020, 226: 106887.
[27] AZHARI-SARAY H, SARKARI-KHORRAMI M, NADEMI-BABAHADI A, KASHANI-BOZORG S F. Dissimilar resistance spot welding of 6061-T6 Al alloy/St-12 carbon steel using a high entropy alloy interlayer [J]. Intermetallics, 2020, 124: 106876.
[28] MA Y E, XIA Z C, JIANG R R, LI W. Effect of welding parameters on mechanical and fatigue properties of friction stir welded 2198 T8 Al-lithium alloy joints [J]. Engineering Fracture Mechanics, 2013, 114: 1−11.
[29] SCHWARTZ M. Innovations in materials manufacturing, fabrication, and environmental safety [M]. CRC Press, 2010.
[30] ZHANG D, XIONG J T, MA Y K, JIANG N, LI, J L. Study of microstructure characteristics and corrosion behavior of 2524 Al alloy RFSSW joint [J]. Materials Characterization, 2022, 190: 112057.
[31] ZHANG D, DONG J, XIONG J T, JIANG N, LI J L GUO W. Microstructure characteristics and corrosion behavior of refill friction stir spot welded 7050 Al alloy [J]. Journal of Materials Research and Technology, 2022, 20: 1302−1314.
[32] ZHANG Cheng-hang, CAO Yu, HUANG Guang-jie, ZENG Qing-hui, ZHU Yu-long, HUANG Xin-de, LI Na, LIU Qing. Influence of tool rotational speed on local microstructure, mechanical and corrosion behavior of dissimilar AA2024/7075 joints fabricated by friction stir welding [J]. Journal of Manufacturing Processes, 2020, 49: 214−226.
[33] ZHANG Cheng-hang, HUANG Guang-jie, CAO Yu, ZHU Yu-long, HUANG Xin-de, ZHOU Yi, LI Qi-lei, ZENG Qing-hui, LIU Qing. Microstructure evolution of thermo-mechanically affected zone in dissimilar AA2024/7075 joint produced by friction stir welding [J]. Vacuum, 2020, 179: 109515.
[34] ZHANG C, HUANG G, LIU Q. Quantitative analysis of grain structure and texture evolution of dissimilar AA2024/7075 joints manufactured by friction stir welding [J]. Materials Today Communications, 2021, 26: 101920.
[35] XU W F, LU H J, LI X H, WANG M, MA J, LUO Y X. Microstructure evolution and stress corrosion cracking sensitivity of friction stir welded high strength AA7085 joint [J]. Materials & Design, 2021, 212: 110297.
[36] PARASURAMAN P, SELVARAJAN R, VISVALINGAM B, ILAMURUGAN R, SUBRAMANIAN K. Stir zone stress corrosion cracking behavior of friction stir welded AA7075-T651 Al alloy joints [J]. Corrosion Reviews, 2021, 39(1): 55−62.
[37] MORETO J A, DOS SANTOS M S, FERREIRA M O A, CARVALHO G S, GELAMOR V, AOKI I V, TARYBA M, BOSE FILHO W W, FERNANDES J C S. Corrosion and corrosion-fatigue synergism on the base metal and nugget zone of the 2524-T3 Al alloy joined by FSW process [J]. Corrosion Science, 2021, 182: 109253.
[38] DENG C, WANG C, WANG F, SONG B, ZHANG H. Effect of microstructure evolution on corrosion behavior of 2195 Al−Li alloy friction stir welding joint [J]. Materials Characterization, 2022, 184: 111652.

异种铝合金回填式搅拌摩擦点焊接头的微观结构演变和腐蚀行为

蒋方圆[1,2]，张 达[1,2]，马艳坤[1,2]，熊江涛[1,2]，郭 伟[1,2]，李京龙[1,2]

1. 西北工业大学 凝固技术国家重点实验室，西安 710072；
2. 西北工业大学 摩擦焊接技术陕西省重点实验室，西安 710072

摘 要：通过回填式搅拌摩擦点焊(RFSSW)制备了异种 2B06 和 7B04 铝合金接头，并研究了接头的微观结构演变和腐蚀行为。根据微观结构分析，焊接接头呈现出不同的微观结构区，包括搅拌区(SZ)、热力影响区(TMAZ)和热影响区(HAZ)，各区域的晶粒大小依次为 HAZ>TMAZ>SZ。与 SZ 相比，TMAZ 和 HAZ 中的第二相颗粒要大得多，而且 HAZ 中的第二相颗粒随着转速的增加而增大。电化学测试表明，腐蚀敏感性依次为 HAZ>TMAZ> SZ> BM，转速越高，敏感性越高。腐蚀后力学性能会下降，主要是由于连接重叠处的缝隙腐蚀，而不是微观结构的变化。

关键词：回填式搅拌摩擦点焊；高强度铝合金；异种接头；微观结构演变；腐蚀行为

(Edited by Bing YANG)